Biodistribution of Different Sized Nanoparticles Assessed by Positron Emission Tomography: A General Strategy for Direct Activation of Metal Oxide Particles

Carlos Pérez-Campaña,[†,‡] Vanessa Gómez-Vallejo,[†,‡] Maria Puigivila,[†,‡] Abraham Martín,[‡] Teresa Calvo-Fernández,[§] Sergio E. Moya,[⊥] Ronald F. Ziolo,[∥] Torsten Reese,[¶,*] and Jordi Llop[†,*]

[†]Radiochemistry Department, [‡]Molecular Imaging Unit, [§]Animal Facility, and [⊥]Biosurfaces Unit, CIC biomaGUNE, San Sebastian, Spain, [∥]Advanced Materials Department, CIQA, Saltillo, Mexico, and [¶]Magnetic Resonance Imaging Department, Molecular Imaging Unit, CIC biomaGUNE, San Sebastian, Spain

ABSTRACT

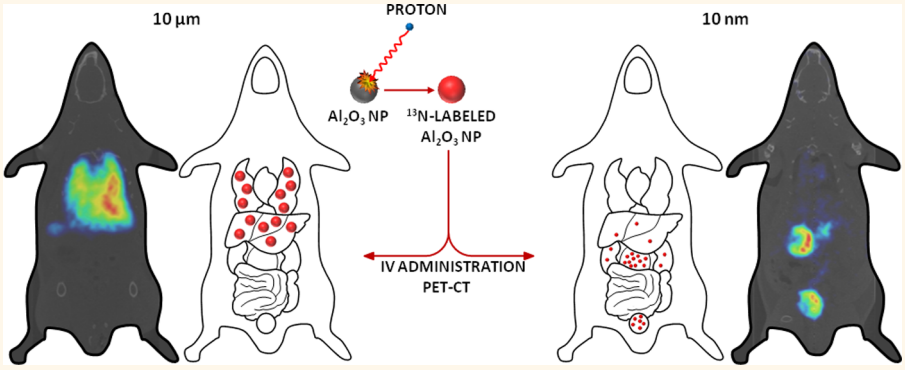

The extraordinary small size of NPs makes them difficult to detect and quantify once distributed in a material or biological system. We present a simple and straightforward method for the direct proton beam activation of synthetic or commercially available aluminum oxide NPs (Al_2O_3 NPs) *via* the $^{16}O(p,\alpha)^{13}N$ nuclear reaction in order to assess their biological fate using positron emission tomography (PET). The radiolabeling of the NPs does not alter their surface or structural properties as demonstrated by TEM, DLS, and ζ-potential measurements. The incorporation of radioactive ^{13}N atoms in the Al_2O_3 NPs allowed the study of the biodistribution of the metal oxide NPs in rats after intravenous administration *via* PET. Despite the short half-life of ^{13}N (9.97 min), the accumulation of NPs in different organs could be measured during the first 68 min after administration. The percentage amount of radioactivity per organ was calculated to evaluate the relative amount of NPs per organ. This simple and robust activation strategy can be applied to any synthetic or commercially available metal oxide particle.

KEYWORDS: positron emission tomography · metal oxide · nanoparticle · nitrogen-13 · proton activation · labeled Al_2O_3

Metal oxide nanoparticles (NPs) have broad applications in industry and in the manufacture of both commercial and personal health care products. Metal oxide NPs are utilized in food or paint additives,[1,2] in the construction and semiconductor industries,[3,4] in cosmetics,[5] solar cells,[6,7] and in many other industrial and societal sectors.

The rapid and ever expanding development of nanotechnology and the increasing incorporation of NPs into everyday products has raised many concerns about their possible risks for human health and the environment.[8−10] One particularly problematic aspect regarding NP safety is the assessment of their biological fate. NPs are extremely difficult to detect and quantify once distributed in a material or biological system.[11] One possibility to overcome this problem consists of labeling the NPs with radionuclides that can lead to their

* Address correspondence to treese@cicbiomagune.es, jllop@cicbiomagune.es.

Received for review January 28, 2013 and accepted March 8, 2013.

Published online March 08, 2013
10.1021/nn400450p

detection in biological systems by means of ultrahigh sensitivity techniques such as positron emission tomography (PET) or single-photon emission-computerized tomography (SPECT) as is routinely done for pharmaceutical compounds.

To date, different strategies for the incorporation of radionuclides into NPs have been developed. A common strategy for NP labeling is the attachment of an appropriate radiolabeled tag to the NP surface.[12−14] While in many cases this is a viable option, the surface chemistry of the NP is modified by the presence of the tag and, consequently, the physicochemical properties and biological activity of NPs might also be altered; in addition, the radiolabel might detach from the NPs in some environments during biodistribution experiments, resulting in a false evaluation of the NP's location.[15] Other strategies are based on the incorporation of the radioactive isotope in the core of the NP, without significantly changing size, chemical composition, or surface properties. These strategies are particularly suitable for metal and metal oxide NPs. The incorporation of a radioactive isotope in NPs can be achieved by direct irradiation of the material with ions[16,17] or thermal neutrons[18−21] or *via* the utilization of radioactive raw materials in the production process.[22−24]

Recently, we reported a novel and valuable strategy for the activation of ^{18}O-enriched aluminum oxide NPs by irradiation with protons to yield ^{18}F-labeled NPs *via* the ^{18}O(p,n)^{18}F nuclear reaction.[25] The activated NPs allowed the determination of the biodistribution pattern in rodents up to 8 h after intravenous (I.V.) administration. Excellent activation yields were obtained with values of 2.25 ± 0.16 MBq/mg in 6 min beam time, target current = 5 μA, saturation yield = 0.45 MBq/μA. This strategy, however, is restricted to the activation of ^{18}O-enriched metal oxide NPs, which were produced in milligram quantities in our laboratory. As such, the enrichment can be costly and time-consuming. Thus, the development of an appropriate methodology for the activation and subsequent study of engineered NPs produced in large quantities for industrial applications or for use in consumer products is highly desirable. In this regard, some studies can be found in the literature in which metal and metal oxide NPs are labeled by the activation of the metallic atom itself.[11] Usually, the production of long-lived gamma or positron emitter radionuclides is pursued since, with such isotopes, the labeled NPs can be monitored over long time periods by either PET or SPECT. However, most of the reported labeling methodologies are case-specific and require irradiation of the NPs for long periods of time to produce a significant amount of labeled NPs.[11]

In the current study, we present for the first time the activation of aluminum oxide (Al_2O_3) NPs by direct irradiation with protons *via* the ^{16}O(p,α)^{13}N nuclear reaction (Figure 1). Sophisticated and costly

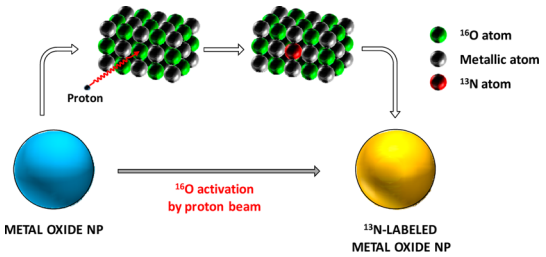

Figure 1. Activation of Al_2O_3 NPs by proton irradiation *via* the ^{16}O(p,α)^{13}N nuclear reaction. Metal oxide NPs are directly irradiated with protons, which convert some of the ^{16}O atoms to ^{13}N atoms by collision. Radioactive atoms are generated throughout the crystal lattice of the NP.

equipment is required; however, despite the short half-life of the ^{13}N atom, 9.97 min, the strategy reported here produced high amounts of radioactivity (1.85 MBq/mg) while implementing short irradiation times (6 min). In addition, this route of activation can be applied to any synthetic or commercially available metal oxide NP irrespective of the metallic atom. We show that the activation of the NPs does not affect the structural or other properties of the NPs. Therefore, valuable information about the biological fate of NPs employed in commercial formulations can be obtained rapidly and easily, especially for fast preliminary screening of a biodistribution pattern of metal oxide NPs depending on, for example, particle size distribution, chemical composition, surface charge, or crystalline phase. Although the residence time of NPs in the body might be much longer than the radioactivation time due to the short half-life of ^{13}N, the initial biodistribution pattern during the first minutes after administration can be easily obtained, as long as the NPs stay unaltered within the body. The present work clearly demonstrates this concept using *in vivo* PET biodistribution studies performed in rodents following I.V. administration of the labeled NPs.

RESULTS AND DISCUSSION

Activation and Characterization of the NPs. In our recent report on the activation of metal oxide NPs to generate a positron emitter in the NP core,[25] ^{18}O-enriched NPs were first synthesized in the laboratory, activated *via* the ^{18}O(p,n)^{18}F nuclear reaction, and their biodistribution pattern was assessed in rats using PET. From this work, three conclusions were drawn: (i) the crystalline phase and the size of the NPs were not affected by the irradiation process; (ii) a short-term biodistribution pattern of the NPs 8 h after administration in rodents could be assessed; and (iii) a plateau was reached in the NP uptake for most of the organs in less than 1 h after administration. These results suggested the possibility of using the shorter-lived positron emitter ^{13}N, which can be generated by irradiation of abundant ^{16}O with protons, to get nearly the same initial macrodistribution information. The advantages of the ^{16}O(p,α)^{13}N route as mentioned in the introduction are that it can

be applied directly to unaltered, large-scale commercial nanomaterials or novel synthetic NPs without the need for costly and time-consuming ^{18}O enrichment.

In the current work, four different aluminum oxide NPs with nominal sizes of 10 nm (NS_{10nm}), 40 nm (NS_{40nm}), 150 nm (NS_{150nm}), and 10 000 nm ($NS_{10\mu m}$) were irradiated with a 16 MeV proton beam (target current = 5 μA, integrated current = 0.5 μAh). As expected, the gamma emission spectrum (Figure 2) showed one band at 511 keV corresponding to positron annihilation; the typical band at 1022 keV (2 $\times$ 511 keV) could also be observed. Aluminum can be activated when exposed to proton irradiation; however, nuclear reactions leading to the formation of long-lived isotopes, such as $^{27}Al(p,3p3n)^{22}Na$ and $^{27}Al(p,p3n)^{24}Na$, have energy thresholds above 20 MeV.[26] The Al_2O_3 NP activation was therefore assigned to nuclear reactions arising from different oxygen isotopes: $^{16}O(p,\alpha)^{13}N$ and $^{18}O(p,n)^{18}F$. For metal oxide particles containing metals that are susceptible to be activated in the 0−16 MeV proton energy range, the formation of other radioisotopes would need to be taken into consideration.

Radiological characterization for the assessment of the relative amount of ^{13}N and ^{18}F produced during irradiation (the latter resulting from activation of ^{18}O, with a relative abundance in naturally occurring oxygen of 0.19%) was performed by fitting a biexponential equation to the curve obtained from dynamic PET scans performed on a small sample of irradiated NPs (Figure 3A). T_1 and T_2 were fixed to half-life values for ^{13}N and ^{18}F, and A_1 and A_2 (amount of radioactivity corresponding to ^{13}N and ^{18}F, respectively) were calculated. Only a 0.5 $\pm$ 0.2% of ^{18}F (corrected for the end of irradiation) was obtained (Figure 3B). However, the longer half-life of ^{18}F with respect to ^{13}N might introduce significant errors into the quantification process during *in vivo* studies, especially at long times after initiating the scan. Thus, a small sample of the irradiated NPs contained in a sealed plastic vial was imaged simultaneously during the biodistribution studies (see below) in order to define the decay curve, which was applied to data correction. Considering the radioisotope ($^{13}N/^{18}F$) relative abundance, the amounts of radioactivity obtained at the end of the irradiation process of NS_{10nm}, NS_{40nm}, NS_{150nm}, and $NS_{10\ \mu m}$ were estimated to be approximately 1.85 MBq/mg, irrespective of NP size. This amount of radioactivity was sufficient in all cases to perform *in vivo* studies.

The stability of the Al_2O_3 NPs after 16 MeV proton irradiation was evaluated by TEM and DLS measurements performed before and after irradiation. TEM images of NPs showed approximately equal average primary particle sizes, within the experimental error, before and after irradiation for all NPs (Table 1). Analysis of individual NP size showed a bimodal distribution for NS_{150nm} NPs with the two NP populations centered around 100 and 180 nm (Figure 4E,F). For NS_{40nm} NPs, a maximum was observed at around 18 nm, but larger NPs (up to 100 nm) were found (Figure 4C,D). NS_{10nm} NPs showed a maximum at around 10 nm, but also in this case, larger NPs were detected (Figure 4A,B). Interestingly, as can be seen in Figure 4A−F, the size distribution of primary particles was not significantly altered during irradiation, irrespective of NP nominal

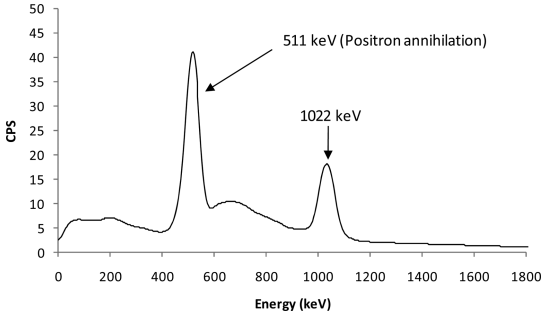

Figure 2. Gamma-ray emission spectrum corresponding to irradiated NS_{10nm} Al_2O_3 NPs. A main peak is observed at 511 keV corresponding to positron annihilation. The peak at 1022 keV (2 $\times$ 511 keV) is also observed. The Compton radiation effect is also detected, with maximum values at ~200 and 600 keV.

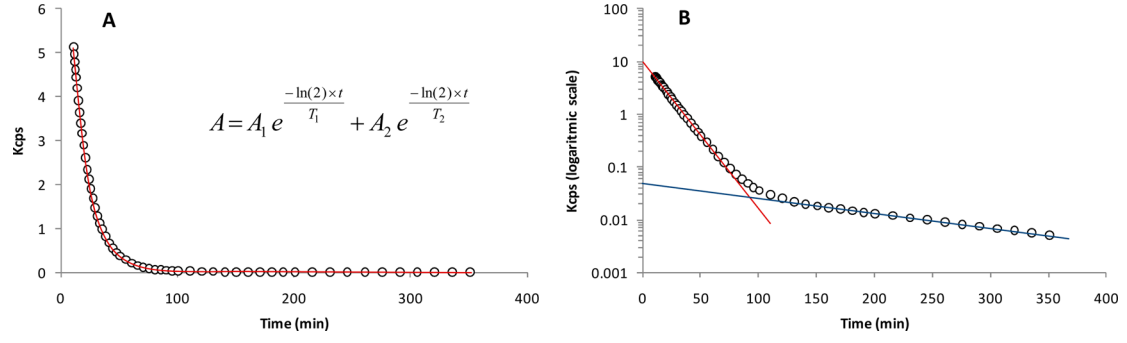

Figure 3. (A) Decay curve of irradiated Al_2O_3NPs (NS_{10nm}) measured with PET; red line corresponds to biexponential curve fitting; white dots are experimental measurements. (B) Decay curve with the *y* axis as a logarithmic scale. The two linear regions correspond to ^{13}N (red line) and ^{18}F (blue line). Intersection of the blue line with *y* axis corresponds to the amount of ^{18}F at the end of irradiation. Intersection of the red line with *y* axis corresponds to the amount of $^{18}F + {}^{13}N$ at the end of irradiation. Slopes of red and blue lines are inversely proportional to half-lives of ^{13}N and ^{18}F, respectively.

TABLE 1. Particle Size (PS) Measured by TEM and DLS and ζ-Potential Values before (BI) and after (AI) Proton Irradiation for NS_{10nm}, NS_{40nm}, NS_{150nm}, and $NS_{10\mu m}$ NPs[a]

	PS (TEM)		PS (DLS)		ζ-potential	
nanoparticle	BI	AI	BI	AI	BI	AI
NS_{10nm}	15(9)	12.2(4.1)	29.2(9.5)	26.7(4.9)	3.3(0.2)	3.2(0.4)
NS_{40nm}	35(20)	31(19)	35.1(8.2)	33.1(8.1)	20.9(1.3)	18.0(3.3)
NS_{150nm}	187(92)	178 ± 68	266.0(19.5)	271.3(18.9)	9.3(0.7)	10.6(2.8)
$NS_{10\mu m}$			2528(225)	2351(109)	−5.7(1.2)	−5.8(1.6)

[a] Mean and standard deviation (in parentheses) values are shown. TEM values were obtained after measuring >300 particles of the same batch before and after irradiation. For DLS and ζ-potential values, three measurements were performed on the same batch, also before and after irradiation. No significant differences were observed among batches within the same nominal particle size.

size. $NS_{10\mu m}$ NPs size could not be accurately determined by TEM.

Slightly larger size values were obtained using DLS for all NPs (Table 1) probably due to the spontaneous formation of aggregates. However, also in this case, measurements performed before and after irradiation offered equivalent results within the experimental error. The ζ-potentials of the NPs (Table 1) were also very similar before and after irradiation. Altogether, these results indicate no significant modification in both particle size and surface charge caused by the irradiation process.

Imaging Studies. Irradiated Al_2O_3 NPs with no further modification were used to assess biodistribution patterns in male rats using PET-CT. After the irradiation process, the radioactive NPs were suspended in a 5 mM NaCl aqueous solution, sonicated for 2 min, and centrifuged at 20*g*. Then, 150−300 μL of the supernatant, equivalent to 10−15 MBq, was withdrawn with a syringe and administered I.V. A smaller fraction (1.5−3 μL, ∼0.1 MBq) was inserted into as plastic vial and imaged simultaneously for decay correction. A third sample of the NPs was allowed to completely decay and was analyzed by DLS to assess the average size of administered NPs. Equivalent values to those shown in Table 1 were obtained.

Biodistribution studies showed a strong size dependency on the distribution and accumulation of NPs in all organs. NP uptake, expressed as percentage of injected dose (%ID) per organ at $6 < t < 10$ (t_{10}) and $60 < t < 68$ (t_{60}) minutes after I.V. administration, is shown in Figure 5A−E.

Accumulation of NPs in the brain was very low, irrespective of particle size (Figure 5A). Although not proven, such low accumulation might be attributable to the contribution of NPs in blood more than real blood brain barrier (BBB) crossing. No significant differences were observed among different sized NPs at a given time point after administration. In addition, results of accumulation at t_{10} were statistically equivalent to the results obtained at t_{60}, suggesting a negligible evolution

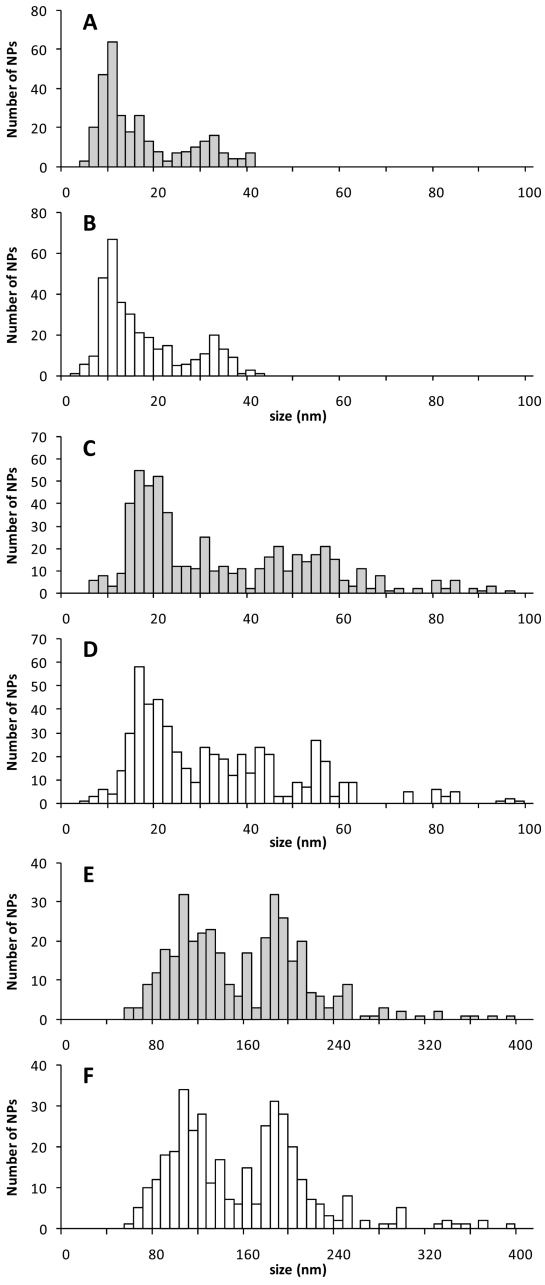

Figure 4. Primary particle size distribution as determined by TEM before (A,C,E) and after (B,D,F) proton irradiation: (A,B) NS_{10nm} NPs; (C,D) NS_{40nm} NPs; (E,F) NS_{150nm} NPs.

of the accumulation of NPs in the brain during the time course of the study, irrespective of particle size.

Very low accumulation (<2%) of NPs was observed in the lungs for NS_{10nm} and NS_{40nm} NPs; this low uptake might also be attributable to the contribution of NPs in blood (Figure 5B). These results are in accordance with our previous findings using ^{18}F-labeled Al_2O_3 NPs, although in that case, smaller particles (5.5 nm as determined by TEM) were used.[25] A significantly higher accumulation was observed when larger NPs were administered. Values around 7% for NS_{150nm} NPs ($P = 0.0146$ *vs* NS_{10nm}, $P = 0.0188$ *vs* NS_{40nm}) and 15% for $NS_{10\mu m}$ NPs ($P = 0.0117$ *vs* NS_{10nm}, $P = 0.0130$ *vs* NS_{40nm})

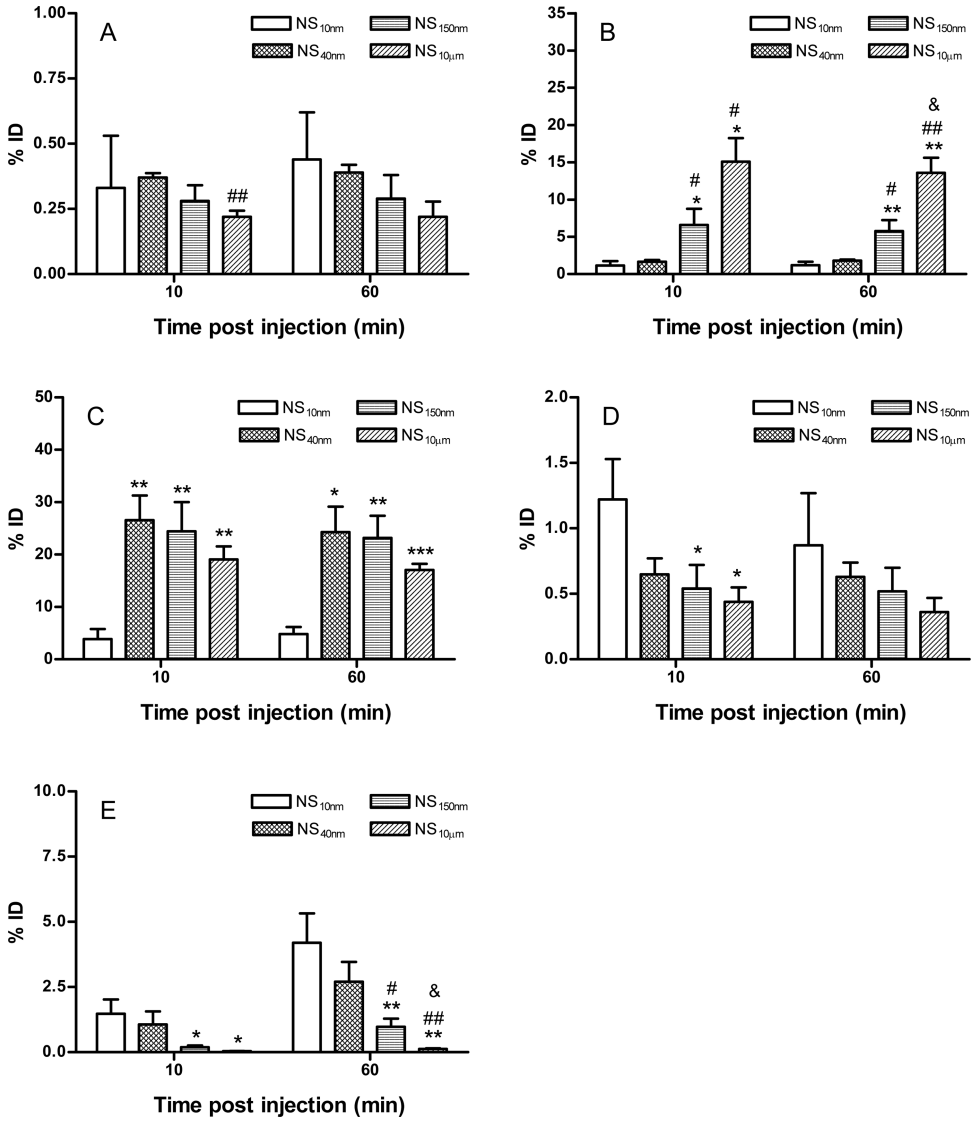

Figure 5. Accumulation of NPs, expressed as percentage of injected dose (%ID) per organ (mean ± standard deviation, $n = 3$) at $6 < t < 10$ (t_{10}) and $60 < t < 68$ (t_{60}) min after I.V. administration; (A) brain; (B) lungs; (C) liver; (D) kidneys; (E) bladder. Within the same time point, statistically different from NS_{10nm} NPs: $^{*}P < 0.05$, $^{**}P < 0.01$ and $^{***}P < 0.001$; statistically different from NS_{40nm} NPs: $^{\#}P < 0.05$ and $^{\#\#}P < 0.01$; statistically different from NS_{150nm} NPs: $^{\&}P < 0.05$.

were found (Figure 5B). The high values obtained for $NS_{10\mu m}$ particles strongly point to NPs being trapped in the capillary pulmonary bed by size exclusion (microemboli of NPs); however, engulfing by phagocytic cells cannot be discounted. The uptake of NS_{150nm} NPs might be explained by spontaneous aggregation of NP post-administration, which could lead also to microemboli of NPs; the presence of large particles (up to 400 nm, see Figure 4F) might also lead to engulfing by phagocytic cells. No significant differences were observed between the uptake values obtained at t_{10} and t_{60}, irrespective of NPs size.

A high proportion of the NPs (~25% for NS_{40nm} and NS_{150nm}, ~20% for $NS_{10\mu m}$; see Figure 5C) accumulated rapidly in the liver. These values can be seen to be significantly higher than uptake values obtained for NS_{10nm} NPs ($P = 0.0096$ *vs* NS_{40nm}, $P = 0.0038$ *vs* NS_{150nm}, $P = 0.0051$ *vs* $NS_{10\mu m}$ NPs). The higher uptake of larger NPs in the liver is in good agreement with phagocytosis by the reticuloendothelial system (RES). The lower, but not significantly different, uptake observed for $NS_{10\mu m}$ with respect to NS_{40nm} and NS_{150nm} might be due to the higher uptake of $NS_{10\mu m}$ in lungs (Figure 5B), which decreases the bioavailability of $NS_{10\mu m}$ NPs.

The accumulation of radioactivity detected in the kidneys (Figure 5D) suggests a slow elimination of smaller NPs (NS_{10nm}) *via* urine. Low accumulation of larger particles might be explained by the high uptake in the lungs due to size exclusion and in other organs by trapping in the RES, which decreases the amount of available NPs for urinary excretion.

The elimination of NPs *via* urine was confirmed by the uptake values in the bladder (Figure 5E).

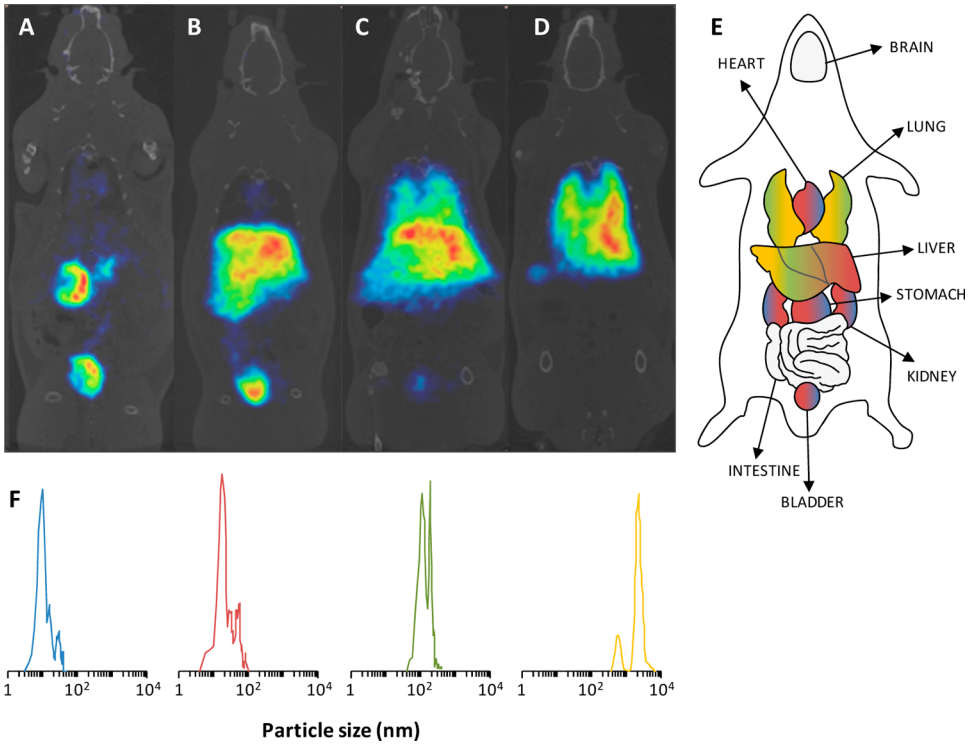

Figure 6. (A−D) PET images of ^{13}N-labeled Al_2O_3 NPs signal at t_{60}: NS_{10nm} NPs (A), NS_{40nm} NPs (B), NS_{150nm} NPs (C), and $NS_{10\mu m}$ NPs (D). Computerized tomography (CT) images were adjusted along the *y* axis for an appropriate fitting with the tracer distribution image. (E) Organ accumulation as a function of particle size, according to color codes depicted in F. (F) Particle size distribution as determined by TEM (NS_{10nm}, NS_{40nm}, NS_{150nm}) or DLS ($NS_{10\mu m}$); gray color in E indicates low accumulation irrespective of particle size.

A nonsignificant increasing tendency was observed with time irrespective of particle size. At t_{10}, the uptake of NS_{10nm} NPs was significantly higher than the uptake observed for NS_{150nm} (P = 0.0303) and $NS_{10\mu m}$ (P = 0.0206). At t_{60}, these significant differences between NS_{10nm} and NS_{150nm} NPs (P = 0.0086) and NS_{10nm} and $NS_{10\mu m}$ NPs (P = 0.0032) were still observed. Values obtained for NS_{40nm} NPs also differed significantly from those of NS_{150nm} (P = 0.0221) and $NS_{10\mu m}$ NPs (P = 0.0042).

In Figure 6, images corresponding to NP uptake in the different organs at t_{60} min are shown (A−D). As can be seen, high accumulation in the liver was observed for NS_{40nm}, NS_{150nm}, and $NS_{10\mu m}$ NPs; accumulation in the lungs was also significant for NS_{150nm} and $NS_{10\mu m}$ NPs, while accumulation in the bladder was observed for NS_{10nm} and NS_{40nm} NPs. In addition, a high accumulation in the stomach was observed for NS_{10nm} and NS_{40nm} NPs. The exact uptake values for the stomach could not be quantified because the anatomical reference of the CT images was not sufficient to draw appropriate volumes of interest (VOIs). Similarly, quantification of NPs in the spleen, an important organ of the RES, was not possible. For those organs not clearly visible in the CT images, co-registration with MRI images might offer an interesting solution. Alternatively, animal sacrifice, organ removal, and subsequent determination of the amount of radioactivity using a gamma counter would also provide relevant data. However, due to invasiveness of the latter, different animals should be utilized to obtain uptake values at different time points after administration. The results obtained from PET images allowed the creation of a distribution pattern, as shown in Figure 6E.

The biodistribution pattern matches with previous results, in which it has been shown that, after injection into the circulatory system, particles are transported along the vasculature and accumulate in different organs through different mechanisms according to particle size. Large particles are trapped in the smallest capillaries of the lungs (>5−7 μm)[27] or engulfed by phagocytic cells in the organs of the RES such as the liver, spleen, and lungs (4−5 μm).[28,29] Smaller particles (10−20 nm) reach various organs by crossing the tight endothelial junctions and are rapidly excreted through the glomeruli of the kidneys.[30,31]

CONCLUSION

In summary, the present study demonstrates that direct irradiation of commercial Al_2O_3 NPs of different sizes with 16 MeV protons allowed sufficient activation through the generation of the positron emitter ^{13}N to perform *in vivo* biodistribution studies *via* I.V. administration in rodents. The accumulation of NPs in the different organs could be determined up to 68 min post-administration. Although the activation time of

the NPs due to the short half life of ^{13}N is shorter than the residence time of the NPs in the body, valuable information concerning the biodistribution pattern during the first minutes post-administration could be obtained. Despite the sophisticated and costly equipment required to perform the experiments, the ease and robustness of the method, together with the fact that it can be applied to any commercially available metal oxide NP, suggest interesting applications in basic biodistribution and fate studies of metal oxide NPs for toxicological or medicinal evaluation. However, it is worth mentioning that assessment of biodistribution after administration of NPs using other routes (*e.g.*, oral, topic, or inhalation) or determination of long-term biological fate might require other approaches like doping the NPs with longer lived isotopes.[11,24]

MATERIALS AND METHODS

Study Design and Statistical Analysis. Four different commercially available Al_2O_3 NPs with nominal sizes 10 nm (NS_{10nm}), 40 nm (NS_{40nm}), 150 nm (NS_{150nm}), and 10 000 nm ($NS_{10\mu m}$) were activated by proton irradiation; morphological studies were used to assess the stability of these NPs under irradiation conditions. The biodistribution pattern was evaluated over a period of 68 min *via* PET following I.V. administration in rats (n = 3 per NP size). Between groups, the concentration of labeled NPs in the different organs was compared by Student's t-test, setting a threshold for statistical significance of $P < 0.05$.

Reagents. All chemicals and solvents were of analytic grade from Sigma-Aldrich, except as noted otherwise. NPs were purchased from Nanostructured and Amorphous Materials, Inc. (NS_{10nm}), PlasmaChem GmbH (NS_{40nm} and NS_{150nm}), and Sigma-Aldrich ($NS_{10\mu m}$). Purified water (ultrapure, type I water, ISO 3696) was obtained from a Milli-Q Integral system (Millipore Iberica S.A.U., Madrid, Spain).

Radioactive Activation of the NPs. Al_2O_3 NPs (70 mg) were placed in an in-house designed aluminum capsule, which was then placed in a solid target holder (Costis, IBA) and irradiated with protons in a Cyclone IBA 18/9 cyclotron with a beam current of 5 μA. The nominal energy of the cyclotron is 18 MeV, which results in a proton energy of ~16 MeV incident on the NPs after the protons pass through a 500 μm aluminum degrader and 100 μm aluminum entrance window in the capsule. An integrated current of 0.5 μAh was used (target current = 5 μA, irradiation time = 6 min).

After irradiation, the capsule containing the activated NPs was automatically inserted into a lead container, which was manually transferred into a 50 mm lead shielded hot cell for subsequent manipulation. The NPs were removed from the capsule, and a small fraction was allowed to decay for structural characterization; a second fraction underwent radiological characterization, and the remaining fraction was used for *in vivo* studies. NPs were suspended in 5 mM NaCl aqueous solution (1 mL), and the suspension was sonicated for 2 min and centrifuged at 20*g* for 4 min to remove aggregates. Then, 150−300 μL of the supernatant (10−15 MBq) was withdrawn with a syringe for administration into animals.

NP Characterization. Size distribution and ζ-potential were determined for all samples before and after irradiation. TEM was performed using a JEOL JEM-1230 microscope operated at 120 kV. With that purpose, Al_2O_3 NP dispersions in hexane were dropped on a 3 mm copper grid covered with a continuous layer of carbon film and were then dried in a vacuum plate degasser overnight. DLS and ζ-potential measurements were performed using a Malvern Zetasizer Nano ZS system.

Activated NPs were also characterized by γ-spectrometry, using a multichannel analyzer γ-spectrometer (MUCHA, Raytest) calibrated with standard energy calibration sources. For radionuclide identification (determination of half-life), a small fraction of the NPs was placed into a specially designed polymethyl methacrylate phantom and inserted in the center of the FOV of an eXploreVista-CT small animal PET-CT system (GE Healthcare). Dynamic images (energy window = 400−700 keV, frames = 10 × 1 min, 10 × 2 min, 10 × 3 min, total acquisition time = 60 min) were acquired, followed by a CT scan for attenuation correction. Images were reconstructed using filtered back projection (FBP) with a ramp filter (cutoff frequency = 0.5 mm^{-1}). VOIs were drawn on the sample cavity, and time−activity curves were obtained as Bq/cm^3. The relative amount of activity present as ^{13}N was estimated by fitting biexponential equations using Origin Pro 8 software.

Animals. Male rats weighing between 240 and 320 g (Sprague−Dawley, Harlan, Udine, Italy) were used to perform PET studies. The animals were cared for and handled in accordance with the Guidelines for Accommodation and Care of Animals (European Convention for the Protection of Vertebrate Animals Used for Experimental and Other Scientific Purposes) and internal guidelines, and experimental procedures were previously approved by local authorities.

Image Acquisition. PET studies were performed using an eXploreVista-CT small animal PET-CT system (GE Healthcare). For each size NP, three animals were submitted to whole body (WB) scans to assess the biodistribution pattern of labeled NPs. In all cases, rats were anesthetized with a mixture of 3−4% isoflurane in O_2 for induction and reduced to 1−1.5% for maintenance in PET by a nose cone to maintain regular breathing at a frequency of 60 ± 10 breaths/min monitored by a pressure sensor (SA Instrument Inc., NY, USA). Respiration and body temperature of the animals were monitored throughout the scan. The temperature, measured rectally, was maintained at 37 ± 1 °C using a water heating blanket (Homeothermic Blanket Control Unit, Bruker, Germany). For administration of ^{13}N-labeled NPs, the tail vein was catheterized with a 24-gauge catheter and 10−15 MBq of NPs (150−300 μL, equivalent to 5−8 mg of NPs) was injected in tandem with the start of a PET dynamic acquisition. A small sample of the irradiated NPs contained in a sealed plastic vial was imaged simultaneously to define the decay curve, and results were applied to data correction.

Dynamic images (13 frames: 3 × 30 s, 3 × 60 s, 3 × 90 s, 4 × 120 s) were acquired in 4 bed positions in the 400−700 keV energy window, with a total acquisition time of 68 min; after each PET scan, CT acquisitions were also performed, providing anatomical information as well as the attenuation map for the later image reconstruction. Dynamic acquisitions were reconstructed (decay and CT-based attenuation corrected) with filtered back projection (FBP) using a ramp filter with a cut off frequency of 1 Hz.

Image Analysis. PET images were analyzed using PMOD image analysis software (PMOD Technologies Ltd., Zürich, Switzerland). Volumes of interest (VOIs) were manually drawn in the lungs, brain, liver, kidneys, and bladder using the CT images as anatomical reference. VOIs were then transferred to the PET images, and the concentration of radioactivity was obtained for each organ and time frame as cps/cm^3. Values were transformed into real activity (Bq/cm^3). Finally, injected dose normalization was applied to data to obtain the percentage of injected dose per organ.

Conflict of Interest: The authors declare no competing financial interest.

Acknowledgment. The authors would like to thank the 7th Framework Program for funding this work through the HINAMOX PROJECT Contract Agreement NMP4-SL-2009-228825, QNANO SP4-Capacities-2010-262163 for support, and Dr. Richard Murray for critical revision of the manuscript.

REFERENCES AND NOTES

1. Zielecka, M.; Bujnowska, E.; Kepska, B.; Wenda, M.; Piotrowska, M. Antimicrobial Additives for Architectural Paints and Impregnates. *Prog. Org. Coat.* **2011**, *72*, 193–201.
2. Blasco, C.; Picó, Y. Determining Nanomaterials in Food. *TrAC, Trends Anal. Chem.* **2011**, *30*, 84–99.
3. Blyszko, J.; Kiernozycki, W.; Guskos, N.; Zolnierkiewicz, G.; Typek, J.; Narkiewicz, U.; Podsiadly, M. Study of Mechanical Properties of Concrete with Low Concentration of Magnetic Nanoparticles. *J. Non-Cryst. Solids* **2008**, *354*, 4515–4518.
4. Stroyuk, A. L.; Shvalagin, V. V.; Kuchmii, S. Y. Photochemical Synthesis and Optical Properties of Binary and Ternary Metal−Semiconductor Composites Based on Zinc Oxide Nanoparticles. *J. Photochem. Photobiol. A* **2005**, *173*, 185–194.
5. Wang, M. C. Synthesis of Zinc Oxide Nanocrystalline Powders for Cosmetic Applications. *Ceram. Int.* **2010**, *36*, 693–698.
6. Yukuphanoglu, F. Synthesis and Electro-optic Properties of Nanosized-Boron Doped Cadmium Oxide Thin Films for Solar Cell Applications. *Sol. Energy* **2011**, *85*, 2704–2709.
7. Sahay, R.; Sundaramurthy, J.; Suresh Kumar, P.; Thavasi, V.; Mhaisalkar, S. G.; Ramakrishna, S. Synthesis and Characterization of CuO Nanofibers, and Investigation for Its Suitability as Blocking Layer in ZnO NPs Based Dye Sensitized Solar Cell and as Photocatalyst in Organic Dye Degradation. *J. Solid State Chem.* **2012**, *186*, 261–267.
8. Weiss, C.; Diabate, S. A Special Issue on Nanotoxicology. *Arch. Toxicol.* **2011**, *85*, 705–706.
9. Ju-Nam, Y.; Lead, J. R. Manufactured Nanoparticles: An Overview of Their Chemistry, Interactions and Potential Environmental Implications. *Sci. Total Environ.* **2008**, *400*, 396–414.
10. Handy, R. D.; von der Kammer, F.; Lead, J. R.; Hassell, M.; Owen, R.; Crane, M. The Ecotoxicology and Chemistry of Manufactured Nanoparticles. *Ecotoxicology* **2008**, *17*, 287–314.
11. Gibson, N.; Holzwarth, U.; Abbas, K.; Simonelli, F.; Kozempel, J.; Cydzik, I.; Cotogno, G.; Bulgheroni, A.; Gilliland, D.; Ponti, J.; *et al.* Radiolabelling of Engineered Nanoparticles for *In Vitro* and *In Vivo* Tracing Applications Using Cyclotron Accelerators. *Arch. Toxicol.* **2011**, *85*, 751–773.
12. Rossin, R.; Pan, D.; Qi, K.; Turner, J. L.; Sun, X.; Wooley, K. L.; Welch, M. J. ^{64}Cu-Labeled Folate-Conjugated Shell Cross-Linked Nanoparticles for Tumor Imaging and Radiotherapy: Synthesis, Radiolabeling, and Biologic Evaluation. *J. Nucl. Med.* **2005**, *46*, 1210–1218.
13. Liang, S.; Wang, Y.; Zhang, C.; Liu, X. Synthesis of Amino-Modified Magnetite Nanoparticles Coated with Hepama-1 and Radiolabeled with ^{188}Re for Bio-magnetically Targeted Radiotherapy. *J. Radioanal. Nucl. Chem.* **2006**, *269*, 3–7.
14. Locatelli, L.; Gil, L.; Limor-Israel, L.; Passoni, L.; Naddaka, M.; Pucci, A.; Reese, T.; Gomez-Vallejo, V.; Milani, P.; Matteoli, M.; *et al.* Biocompatible Nanocomposite for PET/MRI Hybrid Imaging. *Int. J. Nanomed.* **2012**, *7*, 6021–6033.
15. Nemmar, A.; Hoet, P. H. M.; Vanquickenborne, B.; Dinsdale, D.; Thomeer, M.; Hoylaerts, M. F.; Vanbilloen, H.; Mortelmans, L.; Nemery, B. Passage of Inhaled Particles into the Blood Circulation in Humans. *Circulation* **2002**, *105*, 411–414.
16. Chen, J. K.; Shih, M. H.; Peir, J. J.; Liu, C. H.; Chou, F. I.; Lai, W. H.; Chang, L. W.; Lin, P.; Wang, M. Y.; Yang, M. H.; *et al.* The Use of Radioactive Zinc Oxide Nanoparticles in Determination of Their Tissue Concentrations Following Intravenous Administration in Mice. *Analyst* **2010**, *135*, 1742–1746.
17. Leadbeater, T. W.; Parker, D. J.; Gargiuli, J. Positron Imaging Systems for Studying Particulate, Granular and Multiphase Flows. *Particuology* **2012**, *10*, 146–153.
18. Jung, S. H.; Kim, K. I.; Ryu, J. H.; Choi, S. H.; Kim, J. B.; Moon, J. H.; Jin, J. H. Preparation of Radioactive Core−Shell Type ^{198}Au@SiO_2 Nanoparticles as a Radiotracer for Industrial Process Applications. *Appl. Radiat. Isot.* **2010**, *68*, 1025–1029.
19. Roy, J.; Lahiri, S. A Green Method for Synthesis of Radioactive Gold Nanoparticles. *Green Chem.* **2006**, *8*, 1063–1066.
20. Lipka, J.; Semmler-Behnke, M.; Sperling, R. A.; Wenk, A.; Takenaka, S.; Schleh, C.; Kissel, T.; Parak, W. J.; Kreyling, W. G. Biodistribution of PEG-Modified Gold Nanoparticles Following Intratracheal Instillation and Intravenous Injection. *Biomaterials* **2010**, *31*, 6574–6581.
21. Hirn, S.; Semmler-Behnke, M.; Schleh, C.; Wenk, A.; Lipka, J.; Schäffler, M.; Takenaka, S.; Möller, W.; Schmid, G.; Simon, U.; *et al.* Particle Size-Dependent and Surface Charge-Dependent Biodistribution of Gold Nanoparticles after Intravenous Administration. *Eur. J. Pharm. Biopharm.* **2011**, *77*, 407–416.
22. Yang, L.; Sun, M.; Lamichhane, N.; Schutte, J.; Chiao, D.; Sundaresan, G.; Asati, A.; Perez, J. M.; Zweit, J. Synthesis of Different Functionalized ^{141}Ce-Nanoparticle and Their Application in Biological Imaging. *J. Nucl. Med.* **2011**, *52 (supplement 1)*, 1500.
23. Sarparanta, M.; Mäkilä, E.; Heikkilä, T.; Salonen, J.; Kukk, E.; Lehto, V. P.; Santos, H. A.; Hirvonen, J.; Airaksinen, A. J. ^{18}F-Labeled Modified Porous Silicon Particles for Investigation of Drug Delivery Carrier Distribution *in Vivo* with Positron Emission Tomography. *Mol. Pharmaceutics* **2011**, *8*, 1799–1806.
24. Cydzik, I.; Bilewicz, A.; Abbas, K.; Simonelli, F.; Bulgheroni, A.; Holzwarth, U.; Gibson, N. A Novel Method for Synthesis of ^{56}Co-Radiolabelled Silica Nanoparticles. *J. Nanopart. Res.* **2012**, *14*, 1185.
25. Pérez-Campaña, C.; Gómez-Vallejo, V.; Martín, A.; San Sebastián, E.; Moya, S. E; Reese, T.; Ziolo, R. F.; Llop, J. Tracing Nanoparticles *in Vivo*: A New General Synthesis of Positron Emitting Metal Oxide Nanoparticles by Proton Beam Activation. *Analyst* **2012**, *137*, 4902–4906.
26. Grütter, A. Excitation Functions for Radioactive Isotopes Produced by Proton Bombardment of Cu and Al in the Energy Range of 16 to 70 MeV. *Nucl. Phys. A* **1982**, *383*, 98–108.
27. Slack, J. D.; Kanke, M.; Simmons, G. H.; DeLuca, P. P. Acute Hemodynamic Effects and Blood Pool Kinetics of Polystyrene Microspheres Following Intravenous Administration. *J. Pharm. Sci.* **1981**, *7*, 660–664.
28. Litzinger, D. C.; Buiting, A. M.; van Rooijen, N.; Huang, L. Effect of Liposome Size on the Circulation Time and Intraorgan Distribution of Amphipathic Poly(ethylene glycol)-Containing Liposomes. *Biochim. Biophys. Acta* **1994**, *1190*, 99–107.
29. Herant, M.; Heinrich, V.; Dembo, M. Mechanics of Neutrophil Phagocytosis: Experiments and Quantitative Models. *J. Cell. Sci.* **2006**, *119*, 1903–1913.
30. Choi, H. S.; Liu, W.; Misra, P.; Tanaka, E.; Zimmer, J. P.; Ipe, B. I.; Bawendi, M. G.; Frangioni, J. V. Renal Clearance of Quantum Dots. *Nat. Biotechnol.* **2007**, *25*, 1165–1170.
31. De Jong, W. H.; Hagens, W. I.; Krystek, P. Particle Size-Dependent Organ Distribution of Gold Nanoparticles after Intravenous Administration. *Biomaterials* **2008**, *29*, 1912–1919.